

Echoes of Traversable Wormhole

Rajdeep Mondal, Abhishake Sadhukhan

*Department of Physics,
Presidency University,
Kolkata 700073, India*

E-mail: abhishake.physics@presiuniv.ac.in, rajdeepmondal26@gmail.com

ABSTRACT: We study linear scalar perturbations of the four-dimensional, traversable wormhole solution of Maldacena, Milekhin, and Popov[1]. The geometry is constructed by matching an asymptotically flat, near-extremal Reissner–Nordström region to a throat described by $AdS_2 \times S^2$, supported by charged massless fermions. We derive the effective scalar potential governing wave dynamics, which when viewed in the tortoise coordinate, exhibits two extremely sharp and widely separated barriers. These barriers form a resonant cavity and are a direct consequence of the near-horizon geometry of the wormhole mouths. Using time-domain integration, we analyze the wormhole’s response to an initial scalar wave packet inside the throat. We find that the late-time signal contains a distinct train of echoes whose amplitude depends on the angular momentum number l . We show that higher l modes produce significantly stronger echoes, as the corresponding potential barriers are taller and more reflective, which results in more efficient trapping of the wave within the wormhole throat.

Contents

1	Introduction	1
2	Wormhole Geometry	4
2.1	The Wormhole Mouth: A Near-Extremal Geometry	4
2.2	The Wormhole Throat: An $AdS_2 \times S^2$ Geometry	5
3	Scalar Field Perturbations	5
3.1	Perturbation in the Mouth Region	6
3.2	Perturbation in the Throat Region	6
3.3	Matching the Mouth and Throat Geometries	7
4	Scalar Potential in Tortoise Coordinates	9
5	Echoes of the wormhole	12
6	Conclusion and Discussion	15
A	Total energy momentum tensor	17
B	Field Equation Solutions	18

1 Introduction

Wormholes are horizonless structures that can connect two disparate regions of the universe. A key theoretical obstacle to the realization of traversable wormholes in classical general relativity is the violation of the Null Energy Condition [2], which asserts that the energy density experienced by any null observer must be non-negative [3]. Since ordinary matter is expected to satisfy this condition, the construction of a stable, traversable wormhole requires the presence of “exotic” matter with negative energy density, a requirement that points towards the realm of quantum field theory.

The first explicit example of a traversable wormhole consistent with causality was provided by Gao, Jafferis, and Wall [4], who showed that coupling the two boundaries of an eternal AdS black hole produces a violation of the averaged null energy condition from a quantum stress tensor, rendering the wormhole traversable without introducing closed timelike curves. Maldacena, Milekhin, and Popov (MMP) later proposed an explicit four-dimensional traversable wormhole solution within an Einstein–Maxwell theory coupled to charged massless fermions [1]. In this framework, the negative energy density is not postulated ad hoc but emerges dynamically from the one-loop contribution of the fermion fields propagating in the background magnetic field of two near-extremal black

holes. This Casimir-like effect violates the NEC, allowing the wormhole throat to remain open without leading to causality violations in the ambient spacetime. The resulting near-horizon geometry, described by $AdS_2 \times S^2$, is of particular interest as AdS_2 gravity is conjectured to be dual to Sachdev-Ye-Kitaev(SYK) model[5, 6]. While this work provided the first concrete four-dimensional solution, it is conceptually related to the earlier construction by Maldacena and Qi [7] of an eternal traversable wormhole in a nearly AdS_2 background. Such traversable wormholes can be viewed as the gravitational dual to two entangled SYK models [8] with a specific interaction, providing a bridge between gravitational dynamics, quantum information, and condensed matter physics. This connection elevates the study of such wormholes from a mere gravitational curiosity to a probe of fundamental quantum dynamics. A related paper explores the possibility of “humanly traversable wormholes”[9] by introducing a dark sector that interacts only gravitationally with the Standard Model, potentially allowing for macroscopic wormholes using the Randall-Sundrum II model. For recent advances in four-dimensional traversable wormhole solutions within the Einstein–Maxwell–Dirac framework, see, for example, [10–13].

The MMP solution provides the first microscopically well-defined four-dimensional traversable wormhole, but it builds on a broad history of earlier theoretical constructions. Foundational models like the Morris-Thorne metric established the classical framework but required exotic matter by postulation [3]. Other approaches have explored solutions arising from higher-dimensional braneworld scenarios [14, 15] or hypothesized stabilization via generic quantum backreaction effects [16]. This makes it a particularly compelling and physically grounded candidate for observational investigation. Among the most promising signatures of horizonless compact objects are gravitational-wave echoes, first proposed for ultracompact objects [17] and later applied to wormholes [18]. Wormhole echoes are late-time repetitions in a waveform caused by waves reflecting from the wormhole’s throat region. The properties of these echoes, such as their amplitude and delay time and frequency are sensitive probes of the object’s geometry, as seen in models like the Damour–Solodukhin wormhole [19]. Therefore, studying the echoes from the MMP wormhole is not just a test for a single abstract model. It provides a concrete opportunity to connect a quantum-field-theoretic wormhole solution to potentially observable gravitational-wave signatures of quantum gravity.

A critical question for a theoretically robust object like the wormhole is how it could be distinguished observationally from a black hole. The answer may lie in the gravitational wave signal following a merger or perturbation. A standard black hole is defined by its event horizon that completely absorbs any incident wave. Its response to a disturbance, known as the ‘ringdown’, is a simple, exponentially decaying signal of quasinormal modes[20], akin to the fading sound of a struck bell. On the other hand, a horizonless object like a wormhole lacks this perfect absorber. The effective potential barrier is generated by the centrifugal potential and spacetime geometry for incoming waves [17]. While part of the initial wave packet scatters off this barrier, a portion can penetrate it and become temporarily trapped in the ‘cavity’ of the wormhole’s throat. This trapped wave then reflects back and forth, leaking out a small fraction of its energy with each bounce. To a distant observer, this leakage manifests as a train of delayed and attenuated ‘echoes’ appearing

in the late-time waveform, with a time delay corresponding to the light-travel time across the throat region [18, 21]. The morphology of this echo train encodes information about the structure of the reflective surface and the depth of the potential well [22]. Detecting echo signals is a formidable task, since they are generally expected to be faint and easily buried in detector noise [23]. Previous tentative searches in LIGO/Virgo data have reported intriguing candidates [24], but none have yet reached statistical significance [25]. A major limitation of these searches is the lack of theoretically well-motivated templates, which makes it difficult to distinguish genuine signals from noise artifacts. In this work, we take the theoretically robust MMP wormhole geometry and use it as the background to investigate the generation and properties of gravitational-wave echoes. The echo properties we derive such as dependence on angular momentum, time delays, and waveform structure, can serve as the basis for more accurate templates. An eventual detection of such echoes by LIGO, Virgo, or future observatories such as LISA would therefore constitute not only evidence for exotic compact objects, but a direct observational probe of the microphysical dynamics underlying the MMP wormhole geometry. Moreover, the MMP wormhole provides a concrete realization of an AdS_2 throat. Since this geometry is central to the conjectured duality with maximally chaotic SYK-like quantum systems [5, 6], studying its echoes offers a unique opportunity to use gravitational waves as a probe of holographic dynamics. In the wormhole background, perturbations are partially trapped between the effective potential barriers surrounding the throat and gradually leak out as a sequence of echoes. This process can be viewed as a gravitational analogue of how a chaotic quantum system ‘scrambles’ information and eventually thermalizes [26, 27]. Observable features of the echo signal, including its decay rate and characteristic delay, may thus offer a direct probe of quantum thermalization timescales, which may help establish a concrete connection between gravitational-wave signatures and the dynamics of chaotic quantum systems.”

This work investigates the echo phenomenon in the MMP wormhole as a concrete test of whether a quantum-supported traversable geometry naturally produces observational signatures distinct from black holes. As a first step, we study linear perturbations of a massless scalar field. The scalar provides the simplest probe of wave dynamics: it isolates the essential influence of the background geometry without the added complexity of tensorial degrees of freedom. Although actual gravitational-wave observatories are sensitive to tensor perturbations, the echo mechanism which is multiple reflections of perturbations within an effective double-barrier potential, is a generic wave phenomenon common to scalar, electromagnetic, and gravitational fields. Since the effective potential of the MMP wormhole forms a double-well structure with steep, thin barriers, a broad Gaussian wave packet largely transmits through the throat. However, demonstrating scalar echoes confirms that the small fraction of the wave reflected by these barriers is sufficient to sustain the trapping and delayed leakage necessary to generate a distinct echo signal. Our analysis proceeds by deriving the global Schrödinger-like potential obtained by smoothly matching the asymptotically flat exterior to the $AdS_2 \times S^2$ throat, and by showing that it develops the characteristic double-peaked structure of a resonant cavity. Using time-domain finite-difference evolution of Gaussian wave packets, we explicitly identify echo trains and

characterize their morphology. In particular, we study the dependence on the angular momentum number l , thereby checking how different multipoles probe and constrain the quantum-generated structure of the wormhole throat.

The structure of this paper is as follows. In Section 2, we provide a detailed overview of the Maldacena-Milekhin-Popov wormhole geometry, defining the metric in the exterior and throat regions and the procedure for matching them. In Section 3, we introduce the scalar field perturbation, derive the master wave equation, and obtain the effective potentials for the two geometric regions. In section 4, we derive the tortoise coordinates for the wormhole. In Section 5, we present our numerical methodology and the main results of our time-domain simulations, showcasing the echo waveforms and their dependence on the model parameters. Finally, in Section 5, we conclude with a summary of our findings and a discussion of their implications and potential avenues for future research. The appendix([A](#) and [B](#)) contain supplementary details on the derivation of the stress-energy tensor that sources the wormhole solution.

2 Wormhole Geometry

The complete spacetime geometry of the MMP traversable wormhole arises as a solution of the Einstein–Maxwell equations coupled to massless charged fermions [\[1\]](#). Physically, the construction involves two ingredients: the asymptotically flat near-extremal Reissner–Nordström geometry describing the “mouth” region, and the $AdS_2 \times S^2$ throat that develops near the extremal horizon. The latter is supported by the Casimir energy of massless fermions propagating in the background of a magnetic flux. The integer q denotes the magnetic charge, while g is the $U(1)$ gauge coupling constant. These parameters determine both the extremal radius r_e and the characteristic length of the throat. In particular, the wormhole throat length scale is given by

$$L_{\text{wh}} = \frac{16\pi^{3/2}q^2\ell_p}{g^3}, \quad (2.1)$$

where ℓ_p is the Planck length. This scale controls the effective size of the AdS_2 region and will appear explicitly when matching the throat to the mouth geometry in the subsequent subsections.

2.1 The Wormhole Mouth: A Near-Extremal Geometry

We begin with the geometry of the wormhole mouth, which is described by the Reissner–Nordström metric for a magnetically charged black hole [\[1\]](#) of mass M . The metric is given by:

$$ds^2 = - \left(1 - \frac{2MG_N}{r} + \frac{r_e^2}{r^2} \right) dt^2 + \left(1 - \frac{2MG_N}{r} + \frac{r_e^2}{r^2} \right)^{-1} dr^2 + r^2 d\Omega^2 \quad (2.2)$$

The horizons of the metric [\(2.2\)](#) are located at $r_{\pm} = MG_N \pm \sqrt{M^2 G_N^2 - r_e^2}$, where r_+ and r_- are the outer and inner horizons, respectively. The extremal condition, where the two horizons coincide ($r_+ = r_- = r_e$), corresponds to $MG_N = r_e$.

A stable traversable wormhole requires a configuration that is close to, but not exactly, extremal. We therefore work in the near-extremal regime by defining a small, dimensionless parameter ϵ such that:

$$G_N M = r_e + \epsilon \quad (2.3)$$

When $\epsilon > 0$, the object is a black hole with two distinct horizons. When $\epsilon < 0$, there is no horizon, and the geometry can be interpreted as the mouth of a wormhole. Substituting (2.3) into the metric function from (2.2), we can rewrite it as:

$$1 - \frac{2MG_N}{r} + \frac{r_e^2}{r^2} = \left(1 - \frac{r_e}{r}\right)^2 - \frac{2\epsilon}{r} \quad (2.4)$$

This allows us to write the final form of the wormhole mouth metric as:

$$ds^2 = - \left(\left(1 - \frac{r_e}{r}\right)^2 - \frac{2\epsilon}{r} \right) dt^2 + \left(\left(1 - \frac{r_e}{r}\right)^2 - \frac{2\epsilon}{r} \right)^{-1} dr^2 + r^2 d\Omega^2 \quad (2.5)$$

2.2 The Wormhole Throat: An $AdS_2 \times S^2$ Geometry

In the near-horizon limit ($r \rightarrow r_e$), the geometry approaches that of $AdS_2 \times S^2$. The idealized throat metric can be written in (τ, ρ) coordinates as

$$ds^2 = r_e^2 \left[-(\rho^2 + 1) d\tau^2 + \frac{d\rho^2}{\rho^2 + 1} + d\Omega^2 \right]. \quad (2.6)$$

To account for the backreaction from the quantum fermions that support the wormhole throat, one introduces small perturbations $\gamma(\rho)$ and $\phi(\rho)$. The perturbed throat geometry then takes the form

$$ds^2 = r_e^2 \left[-(\rho^2 + 1 + \gamma) d\tau^2 + \frac{d\rho^2}{\rho^2 + 1 + \gamma} + (1 + \phi) d\Omega^2 \right]. \quad (2.7)$$

Following [1], the throat coordinates (τ, ρ) are related to the global (t, r) coordinates of the mouth region by

$$\rho = \frac{L_{\text{wh}}(r - r_e)}{r_e^2}, \quad \tau = \frac{t}{L_{\text{wh}}}, \quad (2.8)$$

Thus, the full perturbed throat metric expressed in (t, r, θ, ϕ) coordinates becomes

$$ds^2 = -\frac{r_e^2}{L_{\text{wh}}^2} (1 + \rho^2 + \gamma(\rho)) dt^2 + \frac{L_{\text{wh}}^2}{r_e^2} \frac{dr^2}{1 + \rho^2 + \gamma(\rho)} + (1 + \phi(\rho)) r_e^2 d\Omega^2, \quad (2.9)$$

with $\rho(r)$ defined as in (2.8). The functions $\gamma(\rho)$ and $\phi(\rho)$ arise from the quantum stress-energy tensor supporting the throat (see Appendix B). This form makes transparent the connection between the throat geometry and the global r -coordinate used for the Reissner–Nordström mouth region, and will allow us to consistently match the two spacetimes.

3 Scalar Field Perturbations

In this section, we derive the master wave equations governing a massless scalar field in the two distinct regions of the wormhole spacetime. Our goal is to obtain a Schrödinger-like equation with an effective potential for each region.

3.1 Perturbation in the Mouth Region

The wormhole mouth region, which connects the asymptotically flat exterior to the throat, is described by the near-extremal Reissner-Nordström metric (2.5). This is a classical solution where we can define a metric function $f(r)$ as:

$$ds^2 = -f(r)dt^2 + f(r)^{-1}dr^2 + r^2d\Omega^2, \quad \text{where} \quad f(r) = \left(1 - \frac{r_e}{r}\right)^2 - \frac{2\epsilon}{r} \quad (3.1)$$

To analyze scalar perturbations, we solve the massless Klein-Gordon equation in this background:

$$\frac{1}{\sqrt{-g}}\partial_\mu (g^{\mu\nu}\sqrt{-g}\partial^\mu\Phi) = 0 \quad (3.2)$$

Given the time-independent and spherically symmetric nature of the background, we can separate the scalar field Φ as follows:

$$\Phi(t, r, \theta, \phi) = \frac{1}{r}\chi(r)Y_{lm}(\theta, \phi)e^{-i\omega t} \quad (3.3)$$

Here, $Y_{lm}(\theta, \phi)$ are the standard spherical harmonics, ω is the frequency of the perturbation, l is the angular momentum quantum number, and $\chi(r)$ is the radial wave function.

Substituting this ansatz into the Klein-Gordon equation (3.2) and introducing the tortoise coordinate r_* , defined by $dr_* = dr/f(r)$, the wave equation reduces to a standard one-dimensional Schrödinger-like form:

$$\frac{d^2\chi(r)}{dr_*^2} + [\omega^2 - V_{\text{mouth}}(r)]\chi(r) = 0 \quad (3.4)$$

The effective potential for the mouth region, $V_{\text{mouth}}(r)$, is given by:

$$V_{\text{mouth}}(r) = f(r)\left[\frac{f'(r)}{r} + \frac{l(l+1)}{r^2}\right] \quad (3.5)$$

where $f'(r)$ denotes the derivative of $f(r)$ with respect to r .

3.2 Perturbation in the Throat Region

Next, we analyze perturbations within the wormhole throat, described by the $AdS_2 \times S^2$ metric with backreaction corrections (2.9). When transformed into (t, r, θ, ϕ) coordinates, this metric takes the form:

$$ds^2 = -f_{th}(r)dt^2 + f_{th}(r)^{-1}dr^2 + h_{th}(r)d\Omega^2 \quad (3.6)$$

Here, the metric functions are defined in terms of the throat coordinate $\rho(r)$ as:

$$f_{th}(r) = \frac{r_e^2}{L_{\text{wh}}^2} (1 + \rho(r)^2 + \gamma(\rho(r))) \quad (3.7)$$

$$h_{th}(r) = r_e^2 (1 + \phi(\rho(r))) \quad (3.8)$$

Due to the radial dependence in the $d\Omega^2$ term via $h_{th}(r)$, the background is not static in the standard sense for the scalar field. This requires a modified ansatz for the scalar field Ψ :

$$\Psi(t, r, \theta, \phi) = \frac{1}{\sqrt{h_{th}(r)}} \zeta(r) Y_{lm}(\theta, \phi) e^{-i\omega t} \quad (3.9)$$

Substituting this into the Klein-Gordon equation (3.2) and defining a new tortoise coordinate for the throat, $dr_* = dr/f_{th}(r)$, we obtain the Schrödinger-like equation for the radial function $\zeta(r)$:

$$\frac{d^2\zeta(r)}{dr_*^2} + [\omega^2 - V_{throat}(r)] \zeta(r) = 0 \quad (3.10)$$

The effective potential for the throat region, $V_{throat}(r)$, is more complex due to the non-trivial function $h_{th}(r)$:

$$V_{throat}(r) = f_{th}(r) \left[\frac{l(l+1)}{h_{th}(r)} - \frac{f_{th}(r)}{4h_{th}(r)^2} (h'_{th}(r))^2 + \frac{f_{th}(r)}{2h_{th}(r)} h''_{th}(r) + \frac{f'_{th}(r)}{2h_{th}(r)} h'_{th}(r) \right] \quad (3.11)$$

The derivatives are taken with respect to the coordinate r . The functional forms of $\gamma(\rho)$ and $\phi(\rho)$ are detailed in [1], and for our numerical work, we use a truncated form of these functions to ensure the tortoise coordinate integration is tractable.

3.3 Matching the Mouth and Throat Geometries

In order to construct the complete wormhole spacetime, it is necessary to consistently join the near-extremal Reissner–Nordström geometry that describes the mouth region with the $AdS_2 \times S^2$ geometry that describes the throat. This requires not only matching of the metric functions at the junction but also ensuring continuity of the effective scalar potential governing perturbations in the combined geometry.

The extremal horizon radius is determined by the magnetic flux through the sphere,

$$r_e^2 = \pi \frac{q^2 \ell_p^2}{g^2}, \quad (3.12)$$

where q is the integer magnetic charge, g is the $U(1)$ gauge coupling, and ℓ_p is the Planck length. For definiteness, we have chosen $\ell_p = 1.6 \times 10^{-33}$ in units where $c = \hbar = 1$. To keep the physical scales r_e of order $O(1)$, we set $q = 10^{33}$. With this normalization, the only undetermined parameters at the junction are the near-extremality parameter ϵ (introduced in (2.3)) and the coupling g .

The matching procedure proceeds as follows: At the junction radius $\tilde{r} = 2.85397$, we impose

$$f_{\text{mouth}}(\tilde{r}) = f_{\text{throat}}(\tilde{r}), \quad (3.13)$$

so that the temporal and radial components of the metric coincide. This ensures that the glued geometry is at least C^0 continuous across the junction. At the same radius, we further require that the angular part of the throat geometry reduces correctly to that of the Reissner–Nordström exterior, namely

$$h_{\text{throat}}(\tilde{r}) = \tilde{r}^2. \quad (3.14)$$

This guarantees smooth continuation of the S^2 sector across the matching surface.

These equations form a closed system that can be solved for the unknowns g and ϵ . Solving numerically in Mathematica, we find

$$g \simeq 1, \quad \epsilon \simeq -4.55934 \times 10^{-15}. \quad (3.15)$$

With these values, the extremal radius from (3.12) is

$$r_e \simeq 2.85365 \quad (3.16)$$

To illustrate the quality of this matching, Fig. 1 shows the radial metric functions $f_{\text{mouth}}(r)$ and $f_{\text{throat}}(r)$ in the vicinity of \tilde{r} , confirming their smooth agreement. We have also constructed the global scalar potential by concatenating $V_{\text{mouth}}(r)$ and $V_{\text{throat}}(r)$ across \tilde{r} (see Fig. 2 for the case $l = 3$). In practice, we find that the effective scalar potential is continuous across the junction for all values of the angular momentum l , with no visible kink at $r = \tilde{r}$.

Finally, we note that our matched parameters, $g \simeq 1$, $q = 10^{33}$, and $\epsilon \simeq -4.559 \times 10^{-15}$, automatically satisfy the stability conditions described in [1]: the negative ϵ guarantees the configuration is horizonless, while the extremely large magnetic charge provides a huge Landau-level degeneracy ($N_{\text{eff}} \sim qN_f \gg 1$ for $N_f = 1$), ensuring sufficient Casimir support for the throat. Also, the matching point satisfies $\tilde{r} - r_e \ll r_e$, confirming that the gluing occurs very close to extremality, and the wormhole length L_{wh} lies well below $q^2\ell_p$ for large q , consistent with semiclassical control. Thus the combined spacetime is a consistent traversable wormhole background.

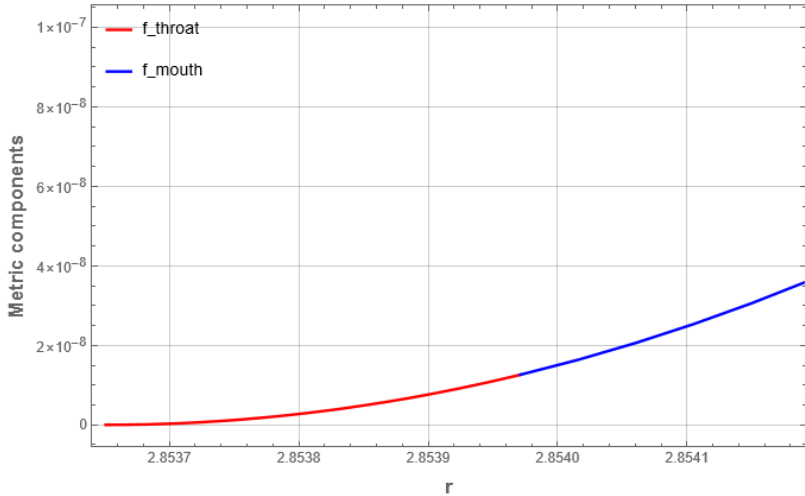


Figure 1: Comparison of the metric functions $f_{\text{mouth}}(r)$ and $f_{\text{throat}}(r)$ in the vicinity of the matching point $r = 2.85397$. The near-coincidence illustrates smooth matching of the geometry.

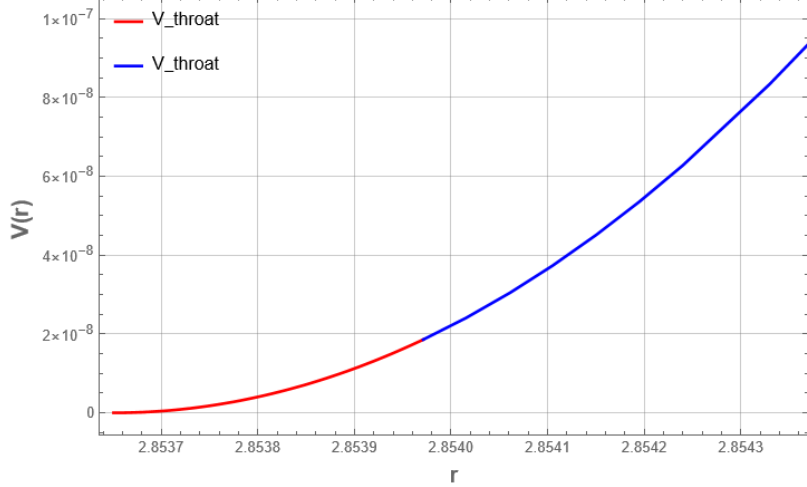


Figure 2: The scalar potential $V(r)$ for $l = 3$ near the matching point $r = 2.85397$, constructed by combining $V_{\text{throat}}(r)$ and $V_{\text{mouth}}(r)$. The potential is nearly continuous across the junction, indicating that wave propagation is well defined globally.

4 Scalar Potential in Tortoise Coordinates

We now construct the effective scalar potential of the wormhole in terms of the tortoise coordinate r_* . Recall that the two regions of the geometry — the Reissner–Nordström mouth and the $AdS_2 \times S^2$ throat — admit separate perturbation equations, given in (3.4) and (3.10), each of which reduces to a Schrödinger-like equation with an effective potential. Our aim is to consistently join these two descriptions and obtain a single global scalar potential, $V_{\text{tot}}(r_*)$, describing the entire wormhole spacetime.

A necessary prerequisite for constructing $V_{\text{tot}}(r_*)$ is to verify the smoothness of the background metric across the junction radius $\tilde{r} = 2.85397$. As discussed in the previous section, at this point, the radial metric functions of the mouth and throat geometries satisfy

$$f_{\text{mouth}}(\tilde{r}) = f_{\text{throat}}(\tilde{r}), \quad h_{\text{throat}}(\tilde{r}) = \tilde{r}^2, \quad (4.1)$$

ensuring continuity of both the temporal–radial sector and the angular sector. Numerically, we find that the difference between the two g_{tt} components at \tilde{r} is negligible. Figure 1 shows the two metric functions plotted in the vicinity of the junction, confirming their smooth agreement.

To glue the two potentials in terms of a common coordinate, we define the tortoise coordinate r_* from

$$\frac{dr_*}{dr} = \frac{1}{f(r)}. \quad (4.2)$$

In the mouth region, this expression becomes

$$r_*^{\text{mouth}}(r) = \int \frac{dr}{f_{\text{mouth}}(r)}, \quad (4.3)$$

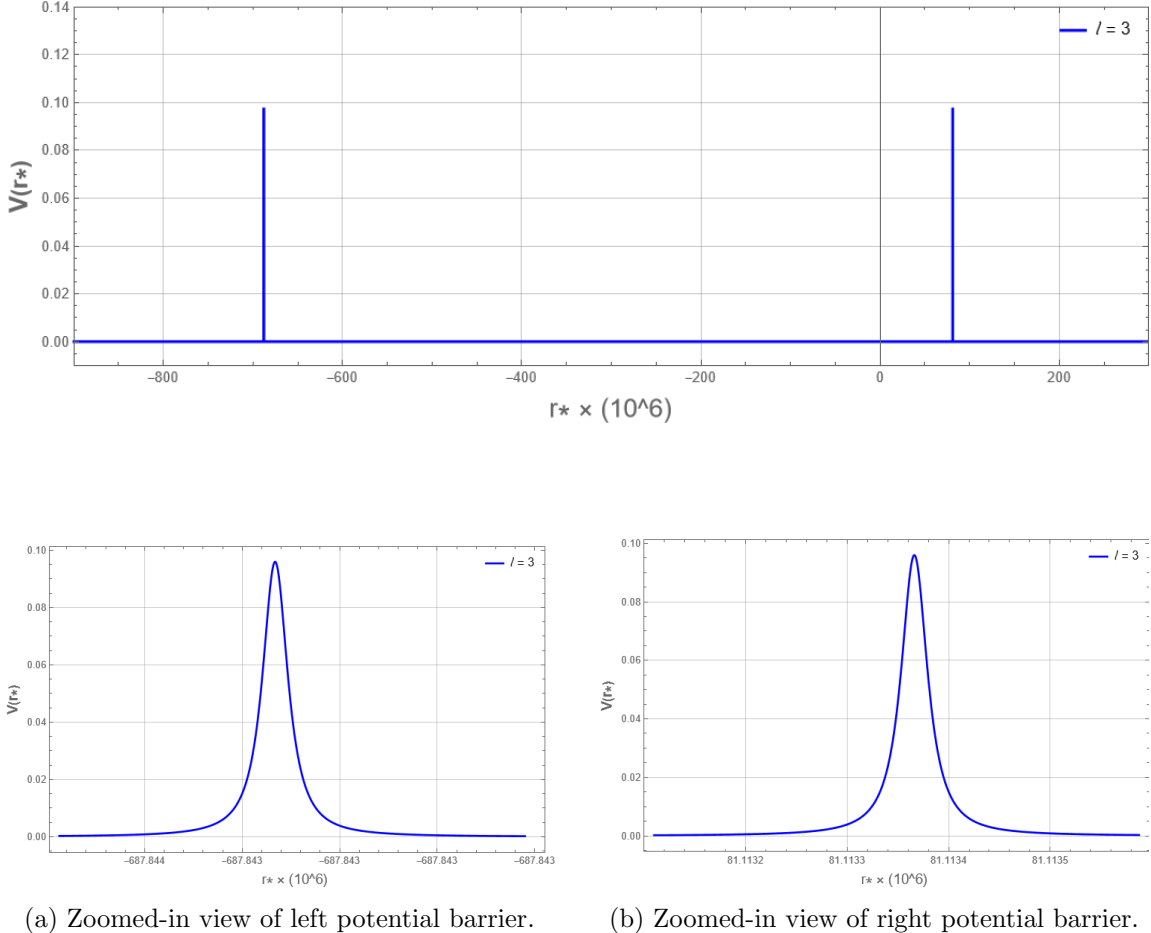


Figure 3: The effective potential for a scalar field with angular momentum $l = 3$ plotted against the tortoise coordinate r_* . The top panel shows the global double-barrier structure, emphasizing the vast separation between the peaks. The bottom panels show magnified views of the (a) left and (b) right barriers, revealing their smooth, bell-like shape.

while in the throat it takes the form

$$r_*^{\text{throat}}(r) = \int \frac{dr}{f_{\text{throat}}(r)}. \quad (4.4)$$

The integration constants on each side are chosen so that

$$r_*^{\text{mouth}}(\tilde{r}) = r_*^{\text{throat}}(\tilde{r}), \quad (4.5)$$

The complete wormhole potential is obtained in two steps. First, we construct the “half-wormhole” potential by joining $V_{\text{throat}}(r)$ from $r = r_e$ up to \tilde{r} and $V_{\text{mouth}}(r)$ from \tilde{r} outward, both expressed in tortoise coordinates. Second, we exploit the reflection symmetry of the throat, $\rho \rightarrow -\rho$, which maps onto $r \rightarrow r_e - (r - r_e)$, to mirror this first half across

r_e . This produces the full wormhole potential with two identical sides smoothly glued at the throat. Figure 3 illustrates this structure for the $l = 3$ mode. The top panel shows the global potential, where the two barriers appear as sharp, widely separated spikes—a direct visual confirmation of the coordinate stretching effect. To reveal their true functional form, the bottom panels provide zoomed-in views of the left (a) and right (b) peaks. These magnified plots make it clear that the potentials are not singular but are in fact smooth, well-behaved, bell-shaped barriers that form the boundaries of the resonant cavity.

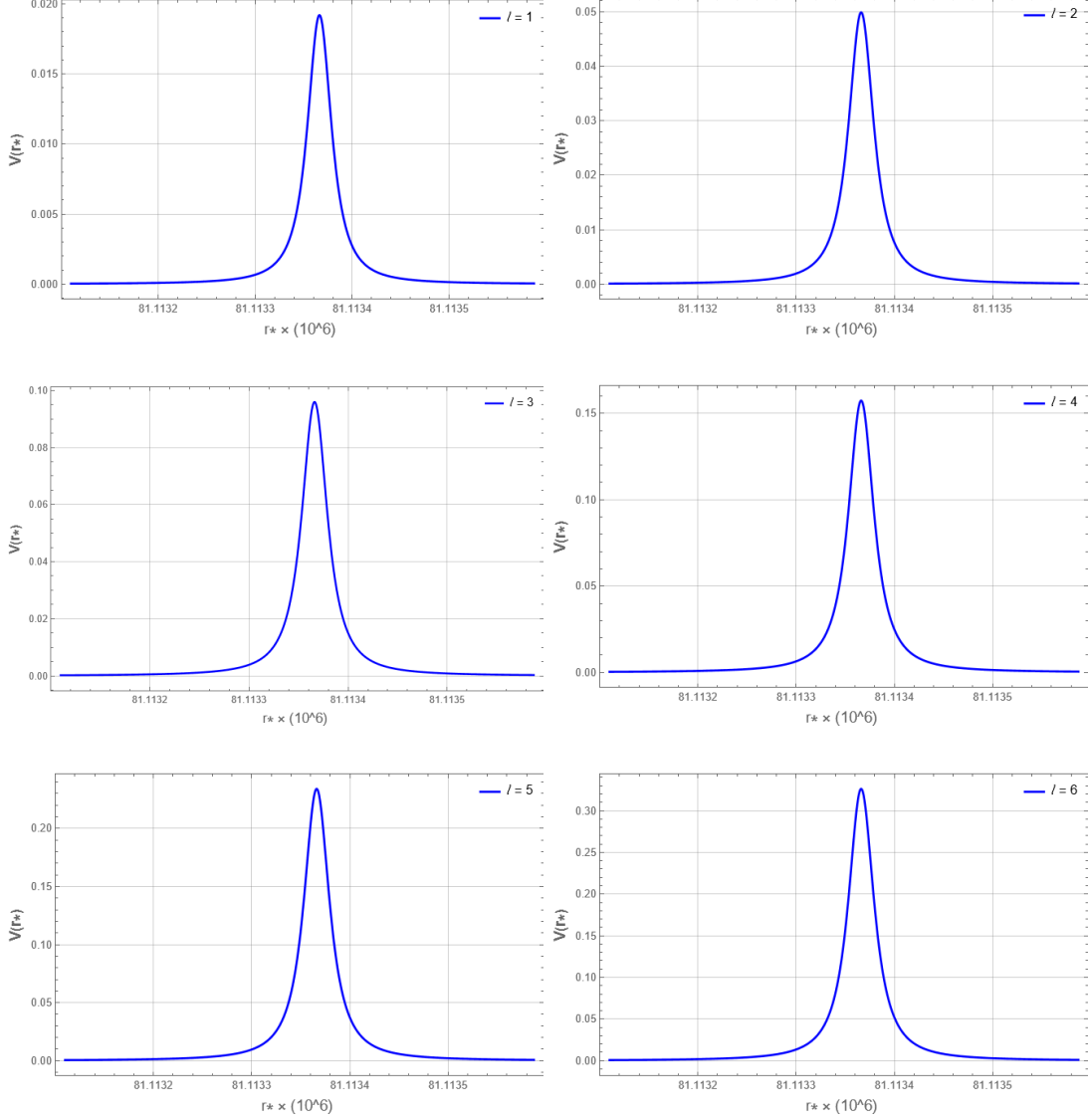


Figure 4: The effective Scalar Potential for angular modes $l = 1$ through $l = 6$.

It is important to note that while the scalar potential $V(r)$ is symmetric about the throat location $r = r_e$. The sharpness of these potential barriers in tortoise coordinates is a key feature that can be traced directly to the near-horizon geometry of the wormhole

mouths. The mouth region is a perturbation of a near-extremal black hole, where the metric function $f(r)$ becomes extremely small. According to the definition of the tortoise coordinate, $dr_* = dr/f(r)$, this implies that a small interval of physical radius Δr near the mouth is exponentially stretched into a vast coordinate distance Δr_* . Consequently, the features of the effective potential, which are physically localized within this narrow radial shell, appear as extremely sharp, almost delta-function-like peaks when plotted as a function of r_* . The height of these barriers is also strongly dependent on the angular momentum number l . For multipolar modes ($l \geq 1$), the potential is dominated by the centrifugal term, $f(r)l(l+1)/r^2$ in (3.5), which creates a significant barrier. In the monopole case ($l = 0$), however, this term vanishes entirely. The remaining potential is comparatively negligible and fails to form a sufficiently high barrier to trap waves effectively. This absence of a resonant cavity for the monopole mode is why prominent echoes are not generated, and we therefore focus our analysis on the cases with $l \geq 1$. Interestingly, the peak positions in r_* are independent of the angular momentum number l , while the peak heights increase monotonically as l grows (Figure 4). This behavior arises from the angular momentum barrier contribution $l(l+1)/r^2$ in the effective potential, which enhances the height of the centrifugal wall without shifting its radial location [28–30].

5 Echoes of the wormhole

We now turn to the numerical study of the time-domain response of scalar perturbations in the traversable wormhole background. As established in the previous sections, the tortoise coordinate r_* spans a vast numerical range, on the order of 10^8 . For computational convenience, all analysis in this section is performed using a rescaled coordinate, where the original r_* values have been scaled down by a factor of 10^6 . Due to the presence of a double-barrier effective potential $V(r_*)$, one expects the appearance of late-time “echoes” in the waveform [12, 30, 31]. To investigate this, we discretize the master wave equation for the scalar field using the finite difference method.

Starting from the general wave equation expressed in tortoise coordinates,

$$-\frac{\partial^2 \psi(t, r_*)}{\partial t^2} + \frac{\partial^2 \psi(t, r_*)}{\partial r_*^2} - V(r_*)\psi(t, r_*) = 0, \quad (5.1)$$

we discretize the solution on a numerical grid,

$$\psi(t, r_*) \rightarrow \psi(i\Delta t, j\Delta r_*) \equiv \psi_{i,j}, \quad V(r_*) \rightarrow V(j\Delta r_*) \equiv V_j,$$

where i and j are integers denoting the time and spatial grid indices. Applying standard centered finite differences to Eq. (5.1) yields

$$-\frac{\psi_{i+1,j} - 2\psi_{i,j} + \psi_{i-1,j}}{\Delta t^2} + \frac{\psi_{i,j+1} - 2\psi_{i,j} + \psi_{i,j-1}}{\Delta r_*^2} - V_j \psi_{i,j} = 0, \quad (5.2)$$

which can be rearranged into an explicit update rule for numerical evolution:

$$\begin{aligned}\psi_{i+1,j} = & -\psi_{i-1,j} + \frac{\Delta t^2}{\Delta r_*^2} (\psi_{i,j+1} + \psi_{i,j-1}) \\ & + \left(2 - 2\frac{\Delta t^2}{\Delta r_*^2} - \Delta t^2 V_j\right) \psi_{i,j}.\end{aligned}\quad (5.3)$$

This finite-difference scheme allows us to evolve $\psi(t, r_*)$ numerically in the time domain. The initial condition is chosen to be a Gaussian wave packet,

$$\psi(0, r_*) = \exp\left[-\frac{(r_* - a)^2}{2b^2}\right], \quad \psi(t < 0, r_*) = 0, \quad (5.4)$$

where a denotes the initial center of the Gaussian and b its width. In our simulations, a is placed outside the double-peak potential region to probe the waveform scattering. Stability of the evolution is ensured by satisfying the CFL condition

$$\frac{\Delta t}{\Delta r_*} < 1,$$

In our simulations, the initial wave packet is placed at the center of the wormhole throat, corresponding to $a = -303$ in tortoise coordinates. The width is set to $b = 2$. This choice is motivated by both physical and computational considerations. Physically, placing the pulse at the center ensures it propagates symmetrically towards both potential barriers, providing a clean probe of the resonant cavity formed between them. The width $b = 1.0$ is narrow enough to be considered a localized pulse, yet broad enough compared to the effective width of the potential peaks to avoid introducing unnecessarily high frequencies. Computationally, this choice represents a practical compromise. The vast coordinate distance separating the potential barriers necessitates a very large numerical grid. A significantly narrower Gaussian (smaller b) would require a prohibitively fine grid spacing Δr_* to be resolved accurately, making the simulation intractable. Thus, $b = 2.0$ allows for a grid resolution that is both stable and computationally feasible. for which we choose $\Delta t = 0.1$ and $\Delta r_* = 0.2$.

The waveform can in principle be extracted at a fixed position either outside the double-peaked potential or within the cavity between the barriers. The detailed shape of the waveform depends on the extraction point, appearing as sharp pulses for an external observer or as trapped ringing for one inside the cavity. However, the echo properties that we study, such as the time delay and oscillation frequency, are fixed by the geometry and are therefore insensitive to the observer's location[32].

The time-domain evolution of the scalar field, reveals the characteristic echo signature expected from a wormhole spacetime. Figure 5 shows the waveform $|\psi(t, r_*)|$ measured by an observer at the center of the wormhole throat($r_* \simeq -3.03 \times 10^8$) for angular momentum modes $l = 1$ through $l = 6$.

The resulting waveform is a train of sharp, distinct pulses. Since the detector is at the origin of the perturbation, the first observed peak is not the initial pulse itself, but

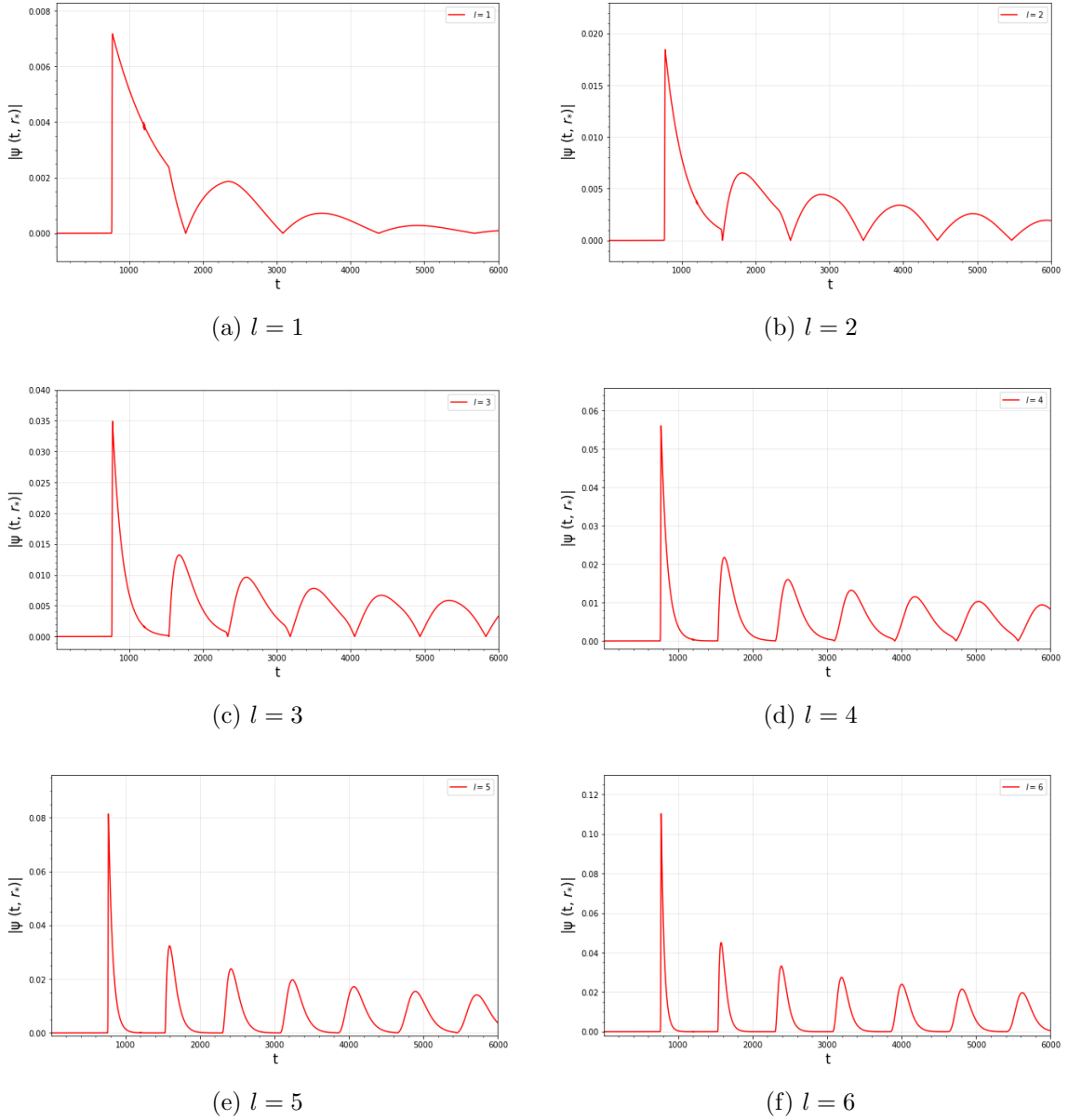


Figure 5: Time-domain profiles of the scalar field response, $|\psi(t, r_* = -303)|$, for angular modes $l = 1$ through $l = 6$. The waveform is measured by an observer at the center of the wormhole throat. The initial pulse is followed by a clear train of echoes, whose amplitude grows significantly with increasing l due to the strengthening of the potential barriers.

rather the first echo. It is formed by the superposition of the two halves of the initial wave packet that have traveled to the potential barriers, reflected, and returned to the center simultaneously. The time delay Δt between consecutive echoes is constant and corresponds to the light travel time across the full length of the wormhole throat in tortoise coordinates.

The signal consists of a series of clean pulses rather than the ringing wave packets seen in some other wormhole studies, is a direct consequence of our initial conditions. The initial Gaussian's width ($b = 2.0$) is much larger than the effective width of the extremely sharp potential barriers. This configuration leads to a direct, coherent reflection of the wave packet, in contrast to studies where a narrower pulse might excite a spectrum of the cavity's quasinormal modes, resulting in a more complex, ringing structure for each echo. Our choice, while computationally necessary, provides a particularly clean probe of the reflection and timing properties of the potential.

The plots also demonstrate the crucial role of angular momentum. As l increases, the height of the potential barriers at the wormhole mouths increases, making them more reflective. This increased reflectivity traps a larger fraction of the wave's energy inside the throat. Consequently, less of the pulse leaks out with each bounce, resulting in a systematically stronger echo signal with higher amplitude peaks, as is evident when comparing the $l = 1$ and $l = 6$ cases. An additional, more subtle feature visible in Figure 5 is the reshaping of the echo pulses as a function of l . For lower angular modes, such as $l = 1$ and $l = 2$, the echo pulses are noticeably broader than for higher modes like $l = 6$, where they appear sharp and narrow. This effect arises from the frequency-dependent nature of wave scattering from the potential barriers. For low l , the potential barrier is relatively short and acts as a "soft" filter. It preferentially reflects the low-frequency components of the initial wave packet while allowing a larger fraction of the high-frequency components to tunnel through and escape. The resulting echo is therefore spectrally dominated by lower frequencies, which corresponds to a wider pulse in the time domain. On the other hand, for high l , the barrier is extremely steep and taller, acting as a "hard" mirror. For all the significant frequencies within the initial wave packet, the barrier's reflectivity is nearly perfect and uniform. As all frequency components are reflected coherently without significant filtering, the shape of the wave packet is well-preserved upon reflection, leading to a sharp, narrow echo pulse. Thus, the very morphology of the echoes encodes detailed information about the shape and steepness of the wormhole's effective potential.

6 Conclusion and Discussion

In this work, we have demonstrated that the four-dimensional Maldacena-Milekhin-Popov traversable wormhole is capable of producing gravitational wave echoes when perturbed. Our central results are twofold. First, we successfully constructed a global, continuous effective potential for a massless scalar field propagating on the MMP background. The metric functions of the mouth and throat regions were explicitly matched at the junction point $\tilde{r} = 2.85397$, ensuring continuity of the geometry. The coordinate interval between \tilde{r} and the extremal radius $r_e \simeq 2.85365$ is extremely small, consistent with the fact that the traversable wormhole metric represents only a slight perturbation of the ex-

tremal Reissner-Nordström black hole, with perturbation parameter ϵ being negative and very small. However, when expressed in terms of the tortoise coordinate, this tiny radial region is highly stretched. Since $r_* = \int dr/f(r)$ and $f(r)$ is suppressed near the throat, the throat region corresponds to a parametrically long interval in r_* , even though it is nearly negligible in r . This reflects the near-extremal character of the solution. The wormhole geometry eliminates the horizon via a negative ϵ , but retains the long throat characteristic of the extremal black hole background. We then imposed mirror symmetry about the wormhole’s central point ($r_e = 2.85365$), which created a symmetric potential well. This “cut-and-paste” construction, inspired by [33], yielded a smooth global potential with the crucial double-barrier structure required for trapping waves.

Second, our time-domain simulations of scalar wave packets evolving in this potential produced a clear train of late-time echoes. This confirms that the MMP geometry inherently supports the echo phenomenon. We observed a strong dependence of the echoes on the scalar angular momentum l . As l increases, the effective potential barrier becomes higher and sharper. This leads to echoes that are generated more easily and their amplitudes are larger. We also observed that the echo pulses become noticeably narrower for higher l modes. For the monopole mode ($l = 0$), echoes are suppressed since the centrifugal barrier term vanishes and only the shallow curvature part of the potential remains, yielding no strong reflection. This predictive relationship between echo morphology and angular momentum is a key characteristic of the model.

These findings have significant implications. They show that that a wormhole model derived from first principles can reproduce observational signatures currently targeted by gravitational-wave searches[24, 34, 35], providing a direct target for improving the templates used in searches by the LIGO-Virgo-KAGRA collaborations[36]. While the echoes are generated by reflection between the two photon-sphere-like barriers, their existence ultimately depends on the presence of the AdS_2 throat supported by fermionic Casimir energy. Since the throat is holographically dual to an SYK-like quantum system, the properties of echoes offer an indirect observational probe into the thermalization dynamics of the dual microstates[26, 27], thereby providing a possible window into the holographic nature of gravity.

This investigation also opens several promising avenues for future research. A natural extension is to move from scalar fields to tensor (gravitational-wave) perturbations, enabling direct waveform templates for LIGO. Another important direction includes incorporating rotation into the wormhole model to investigate superradiant instabilities, which could place stronger constraints on the existence of such objects[37]. Finally, a detailed study of the resonant spectrum in the frequency domain would help to more rigorously connect the echo properties to thermalization timescales in the dual quantum system. Building on this work may provide a new direction to bridge the gap between quantum gravitational theory and observable signatures.

A Total energy momentum tensor

Following [1], the total stress–energy tensor in the MMP wormhole background has two contributions: a classical piece due to the magnetic charge and a quantum contribution representing the negative Casimir energy of massless fermions in the throat. These two sources together determine the backreacted metric functions $\gamma(\rho)$ and $\phi(\rho)$ in the perturbed throat geometry.

The magnetic $U(1)$ gauge field is taken as

$$A = \frac{q}{2} \cos \theta \, d\phi, \quad (\text{A.1})$$

where q is the quantized magnetic charge. The associated field strength is

$$F = dA = -\frac{q}{2} \sin \theta \, d\theta \wedge d\phi, \quad (\text{A.2})$$

so that the nonzero component is

$$F_{\theta\phi} = -\frac{q}{2} \sin \theta. \quad (\text{A.3})$$

The field strength squared is then

$$F_{\theta\phi} F^{\theta\phi} = \frac{q^2}{4(1+\phi)^2}, \quad (\text{A.4})$$

where the $(1+\phi)$ factor arises from the perturbed angular part of the metric.

The classical electromagnetic stress–energy tensor is

$$T^{\mu\nu} = \frac{1}{4\pi} \left(F^\mu{}_\sigma F^{\nu\sigma} - \frac{1}{4} g^{\mu\nu} F_{\alpha\beta} F^{\alpha\beta} \right). \quad (\text{A.5})$$

For instance, the $\phi\phi$ component becomes

$$T^{\phi\phi} = \frac{1}{4\pi} \left(g^{\theta\theta} F_{\theta\phi} F^{\theta\phi} - \frac{1}{4} g^{\phi\phi} F_{\theta\phi} F^{\theta\phi} \right), \quad (\text{A.6})$$

$$= \frac{1}{4\pi} \frac{q^2}{4(1+\phi)^3} \left(\frac{2 \sin^2 \theta - 1}{2 \sin^2 \theta} \right), \quad (\text{A.7})$$

$$T_{\phi\phi} = \frac{1}{4\pi} \frac{q^2}{8(1+\phi)} (2 \sin^2 \theta - 1) \sin^2 \theta. \quad (\text{A.8})$$

Similarly, the $\theta\theta$ component is found to be

$$T_{\theta\theta} = \frac{1}{4\pi} \frac{q^2}{8(1+\phi)} \left(\frac{2 - \sin^2 \theta}{\sin^2 \theta} \right). \quad (\text{A.9})$$

For the radial component, the nonvanishing contribution is

$$T_{\rho\rho}^{\text{mag}} = -\frac{1}{4\pi} \frac{q^2}{8(1+\phi)^2 (1+\rho^2+\gamma)}. \quad (\text{A.10})$$

In addition to the classical magnetic contribution, the throat of the MMP traversable wormhole is supported by negative Casimir energy from massless fermions. This is incorporated as an effective quantum stress-energy contribution $\hat{T}_{\mu\nu}$, which in the $\tau\tau$ and $\rho\rho$ components takes the form [1]:

$$\hat{T}_{\tau\tau} = -\frac{q}{8\pi} \frac{1}{4\pi r_e^2}, \quad \hat{T}_{\rho\rho} = \frac{\hat{T}_{\tau\tau}}{(1+\rho^2)^2}. \quad (\text{A.11})$$

Explicitly,

$$\hat{T}_{\rho\rho} = -\frac{q}{32\pi^2 r_e^2} \frac{1}{(1+\rho^2)^2}. \quad (\text{A.12})$$

The final $\rho\rho$ and $\theta\theta$ components of the Einstein equations then read

$$R_{\rho\rho} - \frac{1}{2}g_{\rho\rho}R = 8\pi G_N (T_{\rho\rho}^{\text{mag}} + \hat{T}_{\rho\rho}), \quad (\text{A.13})$$

$$R_{\theta\theta} - \frac{1}{2}g_{\theta\theta}R = 8\pi G_N T_{\theta\theta}. \quad (\text{A.14})$$

Solving these equations self-consistently determines the perturbative functions $\gamma(\rho)$ and $\phi(\rho)$ which encode the backreaction of the fermionic quantum fields on the wormhole throat geometry.

B Field Equation Solutions

In this section we outline the solution of the Einstein equations in the perturbed throat geometry, following [1]. The goal is to determine the functions $\phi(\rho)$ and $\gamma(\rho)$ appearing in the throat metric. We begin with the $\rho\rho$ component of the Einstein equation.

Solution from the $\rho\rho$ component

The $\rho\rho$ component of the Einstein tensor takes the form

$$R_{\rho\rho} - \frac{1}{2}g_{\rho\rho}R = \frac{-4 + 2(2\rho + \gamma')\phi' + (1 + \rho^2 + \gamma)(\phi')^2 + 2\phi(-2 + (2\rho + \gamma')\phi')}{4(1 + \rho^2 + \gamma)(1 + \phi)^2}. \quad (\text{B.1})$$

On the right-hand side, we include both the magnetic contribution $T_{\rho\rho}^{\text{mag}}$ and the quantum Casimir contribution $\hat{T}_{\rho\rho}$. These are

$$T_{\rho\rho}^{\text{mag}} = -\frac{1}{4\pi} \frac{q^2}{8(1 + \rho^2 + \gamma)(1 + \phi)^2} \equiv \frac{C}{(1 + \rho^2 + \gamma)(1 + \phi)^2}, \quad C = -\frac{q^2}{32\pi}, \quad (\text{B.2})$$

$$\hat{T}_{\rho\rho} = -\frac{q}{32\pi^2 r_e^2} \frac{1}{(1 + \rho^2)^2}. \quad (\text{B.3})$$

The Einstein equation then reads

$$R_{\rho\rho} - \frac{1}{2}g_{\rho\rho}R = 8\pi G_N (T_{\rho\rho}^{\text{mag}} + \hat{T}_{\rho\rho}). \quad (\text{B.4})$$

Expanding to first order in the perturbations ϕ, γ , and fixing the constant C according to [1] as

$$C = -\frac{1}{8\pi G_N}, \quad (\text{B.5})$$

the resulting equation simplifies to

$$\rho\phi' - \phi = (1 + \rho^2) \left[8\pi G_N \hat{T}_{\rho\rho} \right]. \quad (\text{B.6})$$

This is a first-order ODE for ϕ . Solving it yields

$$\phi(\rho) = \alpha(1 + \rho \arctan \rho), \quad (\text{B.7})$$

where α is a constant determined by matching to the stress-energy.

$$\alpha = \frac{q}{8\pi} \frac{8\pi G_N}{4\pi r_e^2}. \quad (\text{B.8})$$

Comparing the constant normalizations requires

$$\frac{-q^2}{32\pi} = -\frac{1}{8\pi G_N}, \quad \Rightarrow \quad q = \frac{2}{\ell_p}, \quad (\text{B.9})$$

where $\ell_p^2 = G_N$ is the Planck length squared. For the physical case, this gives $q \sim 10^{33}$, consistent with the hierarchy assumed in Sec. 3.3.

Solution from the $\theta\theta$ component

Next consider the $\theta\theta$ component of the Einstein equation,

$$R_{\theta\theta} - \frac{1}{2}g_{\theta\theta}R = 8\pi G_N T_{\theta\theta}, \quad (\text{B.10})$$

with

$$T_{\theta\theta} = \frac{1}{4\pi} \frac{q^2}{8(1 + \phi)} \left(\frac{2 - \sin^2 \theta}{\sin^2 \theta} \right). \quad (\text{B.11})$$

Defining a constant $W \equiv \frac{8\pi G_N q^2}{4\pi \cdot 8}$, and substituting $q^2 = 4/G_N$ as found above, one obtains $W = 1$. After simplification, and setting $\theta = \pi/2$ (so $\csc^2 \theta = 1$) to isolate the dominant dependence as in [1], the equation reduces to

$$\frac{1}{2} \left(\gamma'' + (1 + \rho^2)\phi'' + 2\rho^2\phi' + 2\phi + 2 \right) = (1 - \phi). \quad (\text{B.12})$$

Rearranging,

$$\gamma'' + (1 + \rho^2)\phi'' + 2\rho^2\phi' + 2\phi = 0. \quad (\text{B.13})$$

Solution for $\gamma(\rho)$

Substituting the previously obtained solution for $\phi(\rho)$, the general solution for γ is found to be

$$\gamma(\rho) = Z - \alpha \left[\rho^2 + \rho(3 + \rho^2) \arctan \rho - \log(1 + \rho^2) \right], \quad (\text{B.14})$$

where Z is an integration constant. By imposing the reflection symmetry $\rho \rightarrow -\rho$, Z may be fixed. For large ρ , the asymptotics behave as

$$\gamma(\rho) \sim \alpha \left[-\frac{\pi}{2}\rho^3 - \frac{3\pi}{2}\rho + 2\log \rho + \dots \right]. \quad (\text{B.15})$$

Thus, $\gamma(\rho)$ grows cubically with ρ at large radius, while $\phi(\rho)$ exhibits the expected arctangent dependence, in agreement with the original analysis in [1].

References

- [1] J. Maldacena, A. Milekhin and F. Popov, *Traversable wormholes in four dimensions*, *Class. Quant. Grav.* **40** (2023) 155016 [[1807.04726](#)].
- [2] V.A. Rubakov, *The Null Energy Condition and its violation*, *Phys. Usp.* **57** (2014) 128 [[1401.4024](#)].
- [3] M.S. Morris and K.S. Thorne, *Wormholes in space-time and their use for interstellar travel: A tool for teaching general relativity*, *Am. J. Phys.* **56** (1988) 395.
- [4] P. Gao, D.L. Jafferis and A.C. Wall, *Traversable Wormholes via a Double Trace Deformation*, *JHEP* **12** (2017) 151 [[1608.05687](#)].
- [5] S. Sachdev and J. Ye, *Gapless spin fluid ground state in a random, quantum Heisenberg magnet*, *Phys. Rev. Lett.* **70** (1993) 3339 [[cond-mat/9212030](#)].
- [6] A. Kitaev, *A simple model of quantum holography, KITP strings seminar and Entanglement 2015 program (Feb. 12, April 7, and May 27, 2015)* (<https://online.kitp.ucsb.edu/online/entangled15/>) .
- [7] J. Maldacena and X.-L. Qi, *Eternal traversable wormhole*, [1804.00491](#).
- [8] Y. Chen and P. Zhang, *Entanglement Entropy of Two Coupled SYK Models and Eternal Traversable Wormhole*, *JHEP* **07** (2019) 033 [[1903.10532](#)].
- [9] J. Maldacena and A. Milekhin, *Humanly traversable wormholes*, *Phys. Rev. D* **103** (2021) 066007 [[2008.06618](#)].
- [10] J.L. Blázquez-Salcedo, C. Knoll and E. Radu, *Traversable wormholes in Einstein-Dirac-Maxwell theory*, *Phys. Rev. Lett.* **126** (2021) 101102 [[2010.07317](#)].
- [11] R.A. Konoplya and A. Zhidenko, *Traversable Wormholes in General Relativity*, *Phys. Rev. Lett.* **128** (2022) 091104 [[2106.05034](#)].
- [12] M.S. Churilova, R.A. Konoplya, Z. Stuchlik and A. Zhidenko, *Wormholes without exotic matter: quasinormal modes, echoes and shadows*, *JCAP* **10** (2021) 010 [[2107.05977](#)].
- [13] H.-C. Liu and R.-X. Miao, *Traversable wormholes in AdS and entanglement**, *Chin. Phys. C* **49** (2025) 065105 [[2501.02324](#)].
- [14] M. La Camera, *Wormhole solutions in the Randall-Sundrum scenario*, *Phys. Lett. B* **573** (2003) 27 [[gr-qc/0306017](#)].
- [15] K.A. Bronnikov and S.-W. Kim, *Possible wormholes in a brane world*, *Phys. Rev. D* **67** (2003) 064027 [[gr-qc/0212112](#)].
- [16] D. Hochberg and M. Visser, *The Null energy condition in dynamic wormholes*, *Phys. Rev. Lett.* **81** (1998) 746 [[gr-qc/9802048](#)].
- [17] V. Cardoso, S. Hopper, C.F.B. Macedo, C. Palenzuela and P. Pani, *Gravitational-wave signatures of exotic compact objects and of quantum corrections at the horizon scale*, *Phys. Rev. D* **94** (2016) 084031 [[1608.08637](#)].
- [18] V. Cardoso, E. Franzin and P. Pani, *Is the gravitational-wave ringdown a probe of the event horizon?*, *Phys. Rev. Lett.* **116** (2016) 171101 [[1602.07309](#)].
- [19] W.-L. Qian, Q. Pan, B. Wang and R.-H. Yue, *Late-time tail and echoes of Damour-Solodukhin wormholes*, *Phys. Lett. B* **856** (2024) 138874 [[2402.05485](#)].

[20] E. Berti, V. Cardoso and A.O. Starinets, *Quasinormal modes of black holes and black branes*, *Class. Quant. Grav.* **26** (2009) 163001 [[0905.2975](#)].

[21] R.A. Konoplya and A. Zhidenko, *Wormholes versus black holes: quasinormal ringing at early and late times*, *JCAP* **12** (2016) 043 [[1606.00517](#)].

[22] Z. Mark, A. Zimmerman, S.M. Du and Y. Chen, *A recipe for echoes from exotic compact objects*, *Phys. Rev. D* **96** (2017) 084002 [[1706.06155](#)].

[23] I. Fiori et al., *The Hunt for Environmental Noise in Virgo during the Third Observing Run*, *Galaxies* **8** (2020) 82.

[24] J. Abedi, H. Dykaar and N. Afshordi, *Echoes from the abyss: Tentative evidence for planck-scale structure at black hole horizons*, *Physical Review D* **96** (2017) .

[25] N. Uchikata, T. Narikawa, H. Nakano, N. Sago, H. Tagoshi and T. Tanaka, *Searching for gravitational wave echoes from black hole binary events in the third observing run of LIGO, Virgo, and KAGRA collaborations*, *Phys. Rev. D* **108** (2023) 104040 [[2309.01894](#)].

[26] J. Maldacena, S.H. Shenker and D. Stanford, *A bound on chaos*, *JHEP* **08** (2016) 106 [[1503.01409](#)].

[27] Y. Sekino and L. Susskind, *Fast Scramblers*, *JHEP* **10** (2008) 065 [[0808.2096](#)].

[28] H.T. Cho, A.S. Cornell, J. Doukas and W. Naylor, *Black hole quasinormal modes using the asymptotic iteration method*, *Class. Quant. Grav.* **27** (2010) 155004 [[0912.2740](#)].

[29] R.A. Konoplya and A. Zhidenko, *Quasinormal modes of black holes: From astrophysics to string theory*, *Rev. Mod. Phys.* **83** (2011) 793 [[1102.4014](#)].

[30] H. Liu, P. Liu, Y. Liu, B. Wang and J.-P. Wu, *Echoes from phantom wormholes*, *Phys. Rev. D* **103** (2021) 024006 [[2007.09078](#)].

[31] M.-Y. Ou, M.-Y. Lai and H. Huang, *Echoes from asymmetric wormholes and black bounce*, *Eur. Phys. J. C* **82** (2022) 452 [[2111.13890](#)].

[32] H. Huang, M.-Y. Ou, M.-Y. Lai and H. Lu, *Echoes from classical black holes*, *Phys. Rev. D* **105** (2022) 104049 [[2112.14780](#)].

[33] H. Yang, Z.-W. Xia and Y.-G. Miao, *Echoes and quasi-normal modes of perturbations around Schwarzschild traversable wormholes*, *Eur. Phys. J. C* **85** (2025) 742 [[2406.00377](#)].

[34] LIGO SCIENTIFIC, VIRGO collaboration, *Tests of general relativity with binary black holes from the second LIGO-Virgo gravitational-wave transient catalog*, *Phys. Rev. D* **103** (2021) 122002 [[2010.14529](#)].

[35] J. Abedi, H. Dykaar and N. Afshordi, *Echoes from the Abyss: Tentative evidence for Planck-scale structure at black hole horizons*, *Phys. Rev. D* **96** (2017) 082004 [[1612.00266](#)].

[36] A. Maselli, S.H. Völkel and K.D. Kokkotas, *Parameter estimation of gravitational wave echoes from exotic compact objects*, *Phys. Rev. D* **96** (2017) 064045 [[1708.02217](#)].

[37] R. Brito, V. Cardoso and P. Pani, *Superradiance: New Frontiers in Black Hole Physics*, *Lect. Notes Phys.* **906** (2015) pp.1 [[1501.06570](#)].